Pergamon

J. Mech. Phys. Solids, Vol. 44, No. 5, pp. 801–821, 1996

0022–5096/96 $15.00+0.00

PII S0022–5096(96)00024–S

CRACKING PATTERNS IN METAL–CERAMIC LAMINATES: EFFECTS OF PLASTICITY

M. C. SHAW,†‡ T. W. CLYNE,† A. C. F. COCKS,‡ N. A. FLECK‡ and S. K. PATERAS†

† Department of Materials Science & Metallurgy, Pembroke Street, Cambridge University, Cambridge CB2 3QZ, U.K.

‡ Department of Engineering, Trumpington Street, Cambridge University, Cambridge CB2 1PZ, U.K.

ABSTRACT

Multilayered metal–ceramic composites exhibit unique fracture characteristics that result from the need to reinitiate cracks in adjacent ceramic layers across intact metal layers. Quantitative knowledge of the stress and strain fields around cracked brittle layers is required to predict the fracture modes of such composites. In this paper, two competing fracture modes are analysed for a laminate containing a precrack that spans several layers: fracture is either by co-planar crack growth within the ceramic layers ahead of the initial crack, or, by multiple cracking within the ceramic layers. The appropriate boundary conditions employed in the numerical modelling are determined by comparing finite element predictions with experimental observations of elastic and plastic strain distributions around single cracks in Al/Al_2O_3 laminates using moiré interferometry. It is found that plastic yielding of the metal layers encourages single, co-planar crack growth instead of multiple cracking. This competition between single and multiple cracking is summarised in the form of a fracture map.

1. INTRODUCTION

Before brittle–ductile multilayered composites, or laminates, can be used in engineering components, the relationship between their microstructure and fracture modes must be assessed quantitatively. Of particular importance is the capability to predict whether fracture occurs by the propagation of a low-energy single dominant crack or by high energy multiple cracking within each brittle layer (Fig. 1) (Shaw *et al.*, 1993; Huang *et al.*, 1994; Huang and Zhang 1995; Pateras *et al.*, 1995).

In both cases, it has been shown that tensile and flexural loading of pre-cracked laminates causes nucleation of cracks in intact ceramic layers near the crack tip. Although yielding of the metallic layers lowers the stresses in the intact ceramic layers ahead of the crack tip as compared to a fully elastic system (Chan *et al.*, 1993), the magnitude of the stress relaxation tends to be minor, even with metals of low yield stress, such as aluminium. The most important factor affecting such stress concentrations is the thickness of the metal layer, primarily as a consequence of the increased distance between the crack tip and the next ceramic layer. Although this effect has been confirmed for low-metal volume fraction materials (Shaw *et al.*, 1993),

the situation has not yet been quantitatively assessed for cases where the thickness of the metal layers is greater than that of the ceramic layers.

After cracking of the ceramic layers total failure of the laminate occurs by rupture of the intervening metal layers. Whether or not this involves multiple cracking of individual ceramic layers depends in part on how stress is transferred from the cracked ceramic layers into the remainder of the material (Shaw *et al.*, 1993; Huang *et al.*, 1994; Huang and Zhang, 1995). The present paper represents a first step towards the solution of this problem by treating the limiting case of an initially unloaded, precracked system (Fig. 2) with ceramic layers of deterministic strength. The effects of local variations in the strength of the ceramic layers is treated elsewhere (Shaw, 1995).

2. PROBLEM SPECIFICATION

Consider a laminate geometry that contains two cracks: one of length, a_0 (the precrack), and a second crack, which is considered to have reinitiated in the ceramic layer adjacent to the precrack tip, layer C1 [Fig. 2(a)]. A Cartesian co-ordinate system, (x, y), is defined with its origin at the tip of the precrack; see Fig. 2(a). Previous analyses of this problem have shown that the maximum value of the axial component of stress, σ_{yy}, occurs either ahead of the second renucleated crack, i.e. in ceramic layer C2, which is uncracked [Fig. 2(a)], or above and below the renucleated crack in layer C1 (Shaw *et al.*, 1993; Huang *et al.*, 1994; Huang and Zhang, 1995). The location of this peak stress is dictated by the importance of two roles played by the bridging metal ligament. The first role is to decrease the axial stress in layer C2 by crack bridging, and the second is to increase the stress in layer C1 (Shaw *et al.*, 1993; Huang *et al.*, 1994; Huang and Zhang, 1995). Microstructural parameters affecting the relative magnitudes of the crack tip and wake stresses include the relative thickness of the layers (Shaw *et al.*, 1993; Huang *et al.*, 1994; Huang and Zhang, 1995), and the yield stress of the metal (Huang *et al.*, 1994; Huang and Zhang, 1995). The effect of the length of the precrack, however, is as yet unknown.

Plastic yielding of metal layers M1 (the one that bridges the cracked ceramic layers) and M2 (that separates the tip of the renucleated crack from layer C2) strongly influences the location of the peak axial stress. Plastic flow in layer M1 decreases the crack wake stresses by reducing the magnitude of the surface traction acting on the crack face, and increases the stress in layer C2 due to a loss of crack shielding. Plastic flow in layer M2, however, reduces the stress in layer C2, as described earlier. The ratio of the cracking stress of the ceramic, σ_c, to the flow stress of the metal, σ_y, is therefore an important parameter in determining the location of the peak axial stress (Huang and Zhang, 1995). For example, raising this ratio for cases with an infinite precrack and where the peak axial stress is in the cracked ceramic layer is predicted to shift the location of peak stress to the intact ceramic layer ahead of the crack tip (Huang and Zhang, 1995). However, since there is interest in initial precracks as short as a single ceramic layer thickness, one goal of the present investigation is to determine the effect of such short cracks on the fracture mode. Finally, a primary aim of the present investigation is to examine the validity of finite element analyses by comparing

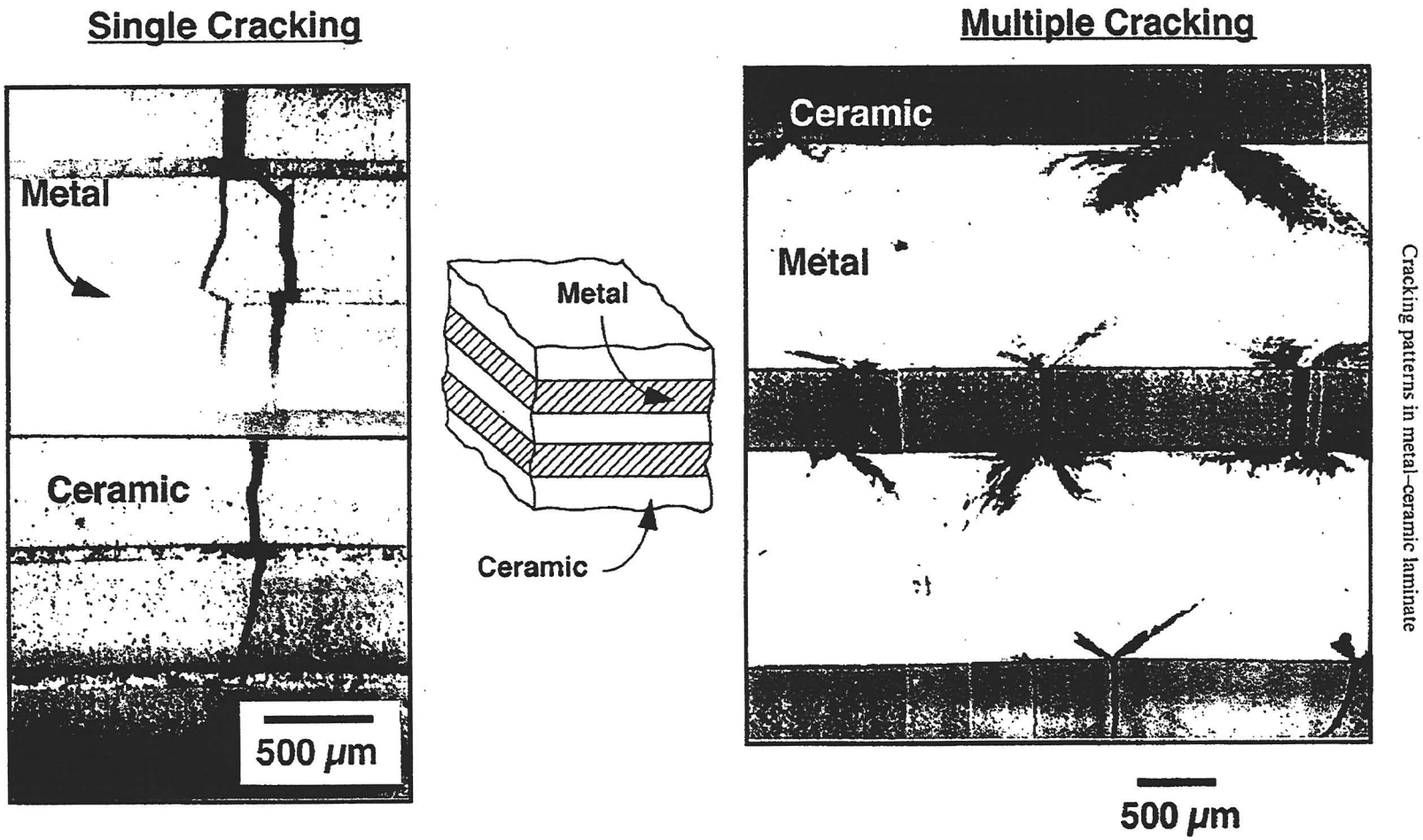

Fig. 1. Optical micrographs of Al/Al_2O_3 laminates exhibiting (a) co-planar, dominant cracking and (b) multiple cracking.

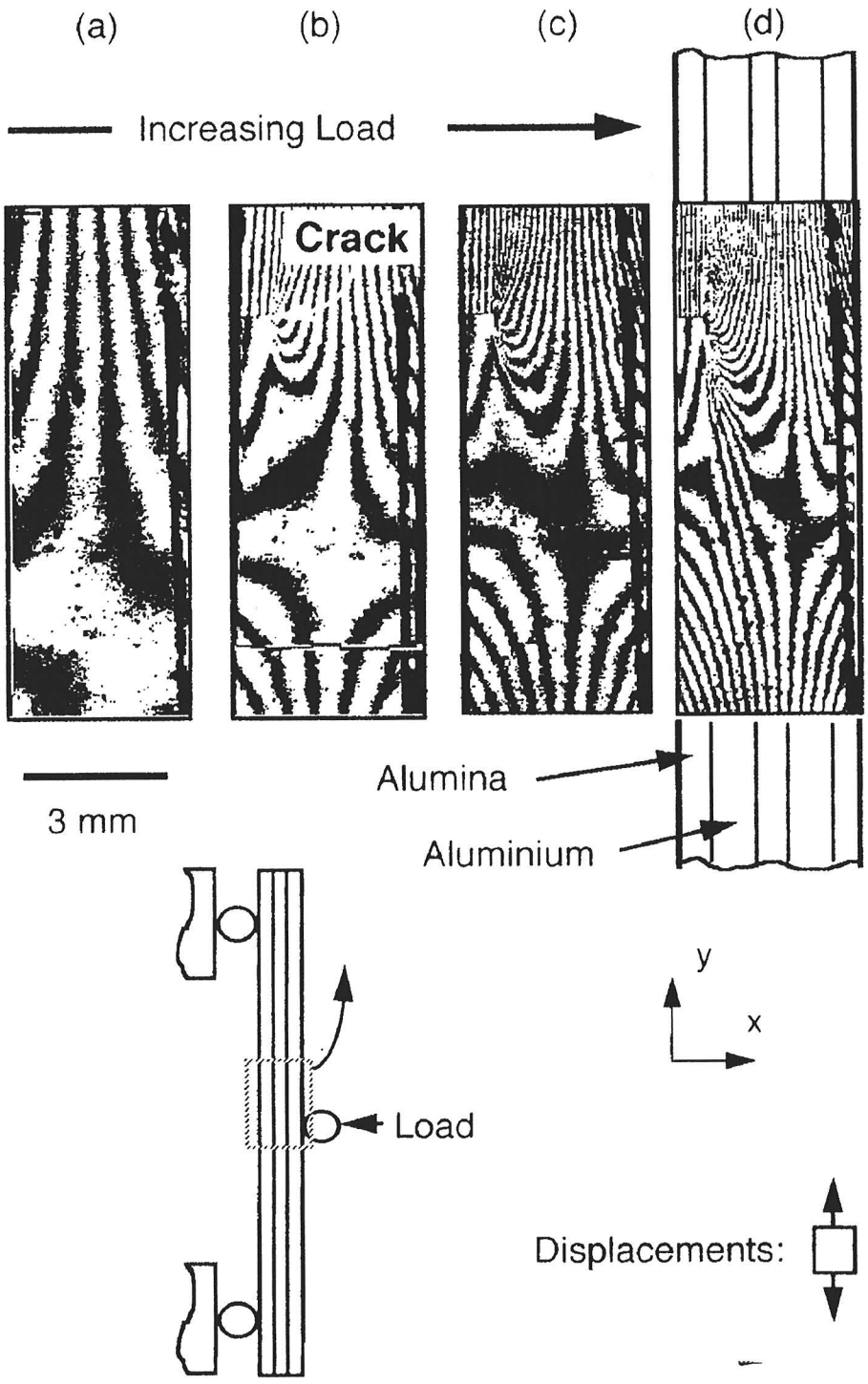

Fig. 3. Moiré interferographs showing longitudinal displacement fields accompanying a flexural experiment described in the text. No cracks are present in (a), whereas a crack has formed in the left ceramic layer in (b) through (d). The fringes correspond to contours of constant displacement in the vertical (y) direction, with a separation of 0.42 μm fringe.

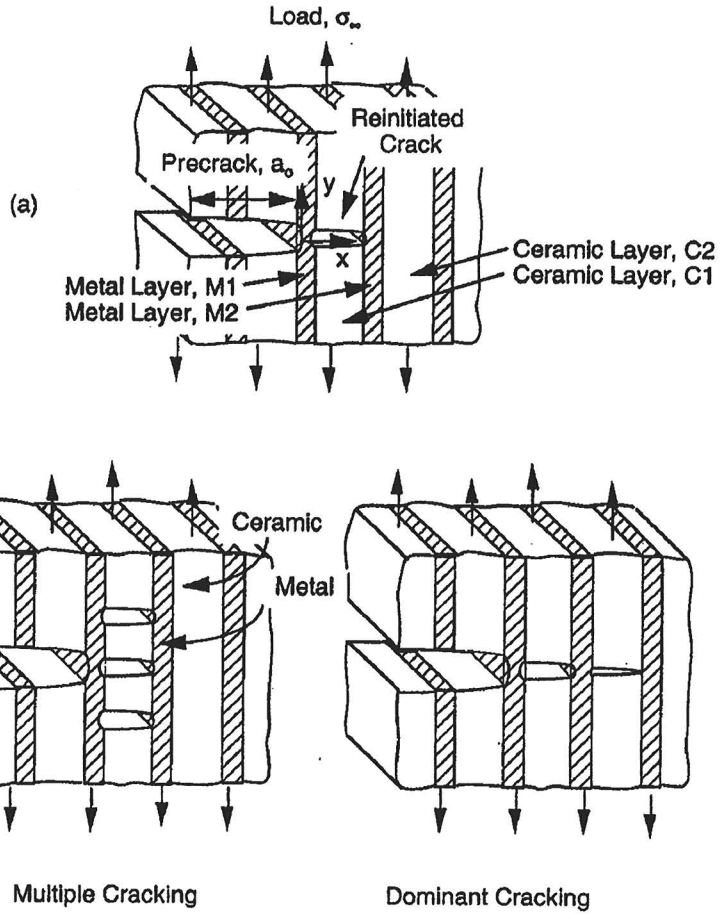

Fig. 2. Schematics illustrating (a) the initial geometry and (b), (c) subsequent cracking modes. The cracking sequence in (b) corresponds to multiple cracking and in (c) corresponds to co-planar dominant cracking.

predictions for crack tip strain fields obtained by finite element analysis with those obtained experimentally by moiré interferometry.

3. STRESS ANALYSIS OF CRACKED, LAYERED GEOMETRIES

In this section we employ the finite element method to determine the stress and strain fields within the different layers of a cracked geometry. Two situations are examined in detail. In Section 3.1, the underlying assumptions of the finite element model are examined by comparing predicted strain fields around a single crack in an Al/Al_2O_3 laminate subject to three point flexural loading with data obtained by moiré interferometry. Particular attention is paid to modelling the crack tip that impinges on the metal layer and the nature of the interfacial bond between the metal and

ceramic layers. In Section 3.2 of the finite element analysis, the stress fields in the vicinity of the precrack tip are determined subject either to remote tensile loading or the asymototic crack-tip displacement field, assuming small-scale yielding. A range of layer thickness ratios, precrack lengths and remote loads are investigated and the results are used to assist in the construction of a fracture map (Section 4).

All the finite element analyses incorporated the following features: (i) only the upper half of the laminate specimen geometry was modelled, by symmetry considerations, (ii) the lateral faces of the mesh are traction-free, (iii) the crack faces are traction-free, (iv) the lower surface of the bridging metal layer, and the uncracked parts of the specimen were constrained against displacement in the vertical (y) direction, but not the horizontal (x) direction. The analyses were conducted using plane strain conditions and a mixture of 8-noded quadrilateral and 6-noded triangular elements. Large deformation analyses with hybrid elements were used with perfect bonding between the layers.

3.1. *Single crack geometry: flexural loading*

3.1.1. *Flexural loading: moiré interferometry experiments.* High-resolution strain mapping experiments were conducted around a single crack in Al/Al_2O_3 laminates subject to three-point flexural loading using moiré interferometry (Post, 1987). A description of the experimental procedure is summarised in the Appendix. Experiments were conducted using aluminium/alumina laminates containing three ceramic layers and two metal layers in three point flexure. The dimensions of the beams used are summarised in Table 1. During initial loading, the beams exhibited a fringe pattern consistent with simple flexure [Fig.3 (a)]. For the case illustrated in Fig. 3, when the strain in the outer ceramic layer reached the value of 8×10^{-4}, a crack initiated in the outer ceramic layer. This crack tunnelled through the layer and arrested at the interface between the ceramic and metal layers. A convergence of fringes was observed in the metal layer in the vicinity of the crack tip, corresponding to a strain intensification within the metal layer associated with the presence of the crack [Fig. 3(b–d)]. As the level of the remote flexural load was increased, the number of fringes increased [Fig. 3(b–d)]. The distribution of axial strain, ε_{yy}, along longitudinal trajectories within the metal and uncracked ceramic layers were determined from the interferographs for comparison with the numerical predictions.

Typical distributions of the axial strain component, ε_{yy}, in the metal layer are

Table 1. *Dimensions of mechanical test specimens (moiré interferometry)*

Outer roller (mm)	40
Specimen height, h (mm)	3.5
Specimen width, b (mm)	4
Number of ceramic layers	3
Number of metal layers	2
Ceramic layer thickness (mm)	0.5
Metal layer thickness (mm)	1.0

plotted as a function of vertical distance from the crack plane in Fig. 4. Results are shown for three trajectories located at positions from the crack tip of 1/4, 1/2 and 3/4 of the metal layer thickness, at a fixed bending moment of 1.5 Nm. These are denoted as trajectories A, B and C, respectively. The strains were not measured experimentally within $\sim 50\ \mu m$ of the crack tip ($0.05\ h_m$), as a result of disintegration of the epoxy diffraction grating within this region. The axial strains in trajectory A were the highest, and decreased for trajectories B and C, which were located further from the crack tip. In all three trajectories, a peak in strain was observed at a distance from the crack plane corresponding to approximately one ceramic layer thickness. The peak axial strain in trajectory A was $\sim 1.3 \times 10^{-3}$. For all three trajectories, the strain then decreased with further distance from the crack plane, until a far-field axial strain was

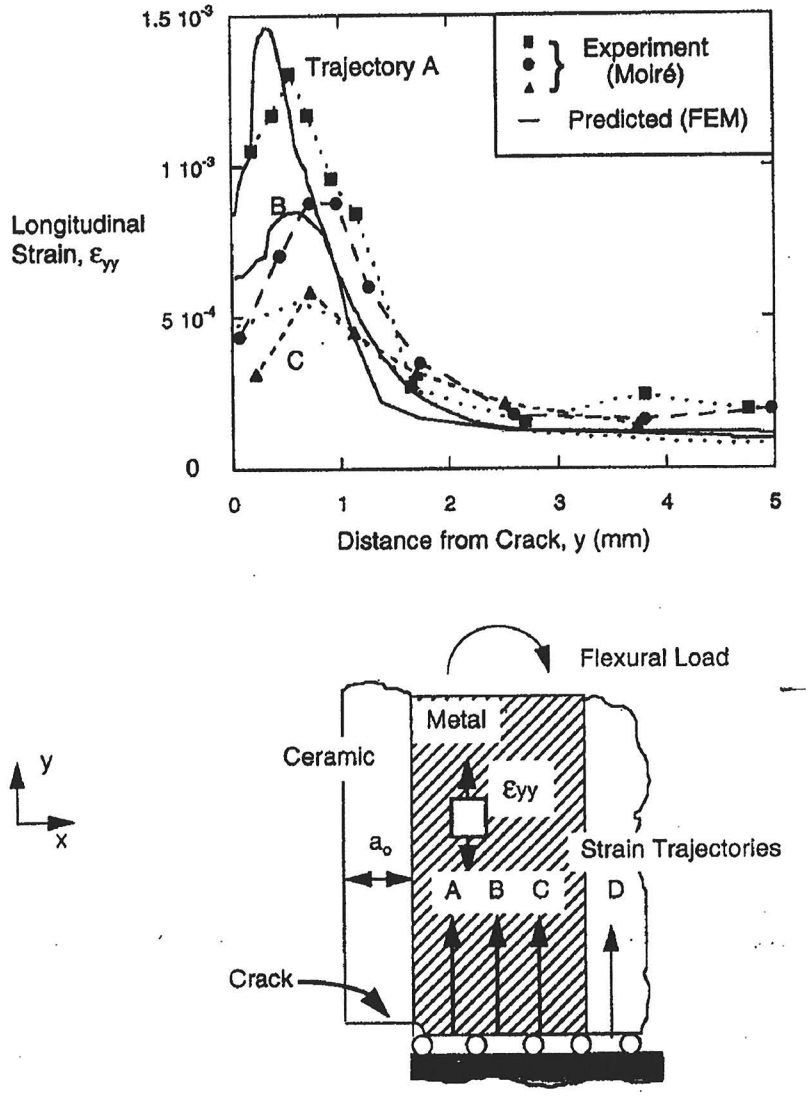

Fig. 4. Distributions of longitudinal strain, ε_{yy}, vs distance from the crack plane, y, within the metal layer along three different trajectories. The applied bending moment is 1.5 Nm. Both experimental measurements and numerical predictions are shown.

reached at a distance of ~2 mm (twice the metal layer thickness). The magnitudes of the steady-state far-field strains were well below the yield strain of the metal and the cracking strain of the ceramic.

The axial strains are plotted in Fig. 5 for two different magnitudes of applied bending moment (1.5 and 2.0 Nm) for trajectory B. The strain distribution for the low load case is the same as in Fig. 4. The magnitude of the peak axial strain within the metal increased by over 100%, from 9×10^{-4} to 2.1×10^{-3}. The distance from the

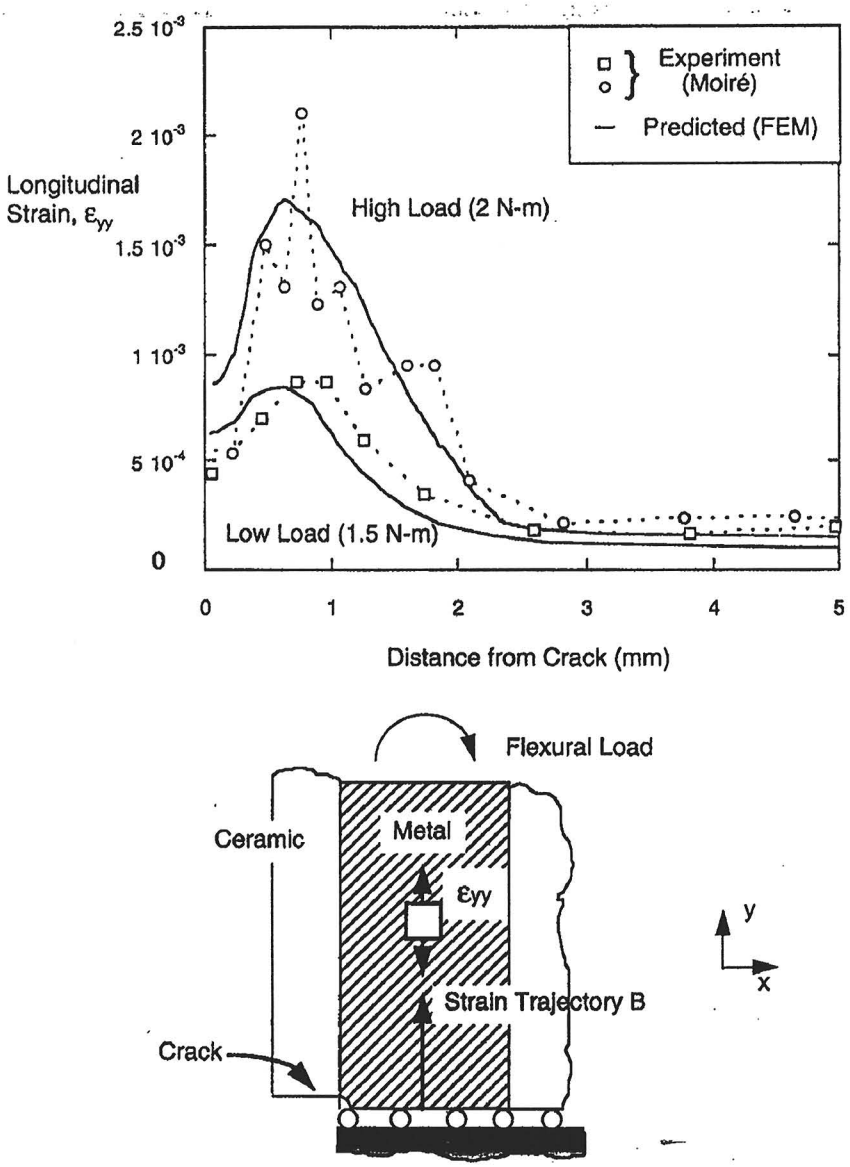

Fig. 5. Distributions of longitudinal strain, ε_{yy}, vs distance from the crack plane, y, along the *middle* of the metal layer for applied bending moments of 1.5 and 2 Nm. Both experimental measurements and numerical predictions are shown.

crack plane over which the strains were increased relative to the remote strains was also greater for the case of a higher remote load.

Finally, the distribution of axial strain along a line $\sim 50\ \mu m$ from the interface within the intact ceramic layer opposite the crack (trajectory D in Fig. 4) is shown in Fig. 6 for two applied bending moments of 2 and 2.8 Nm. Here, the magnitude of the remote axial strains increased as a result of the increased remote load from 1.3×10^{-4} to 2×10^{-4}, and the magnitude of the peak strain within the ceramic increased from 5×10^{-4} to 9×10^{-2}, both approximately by a factor of two.

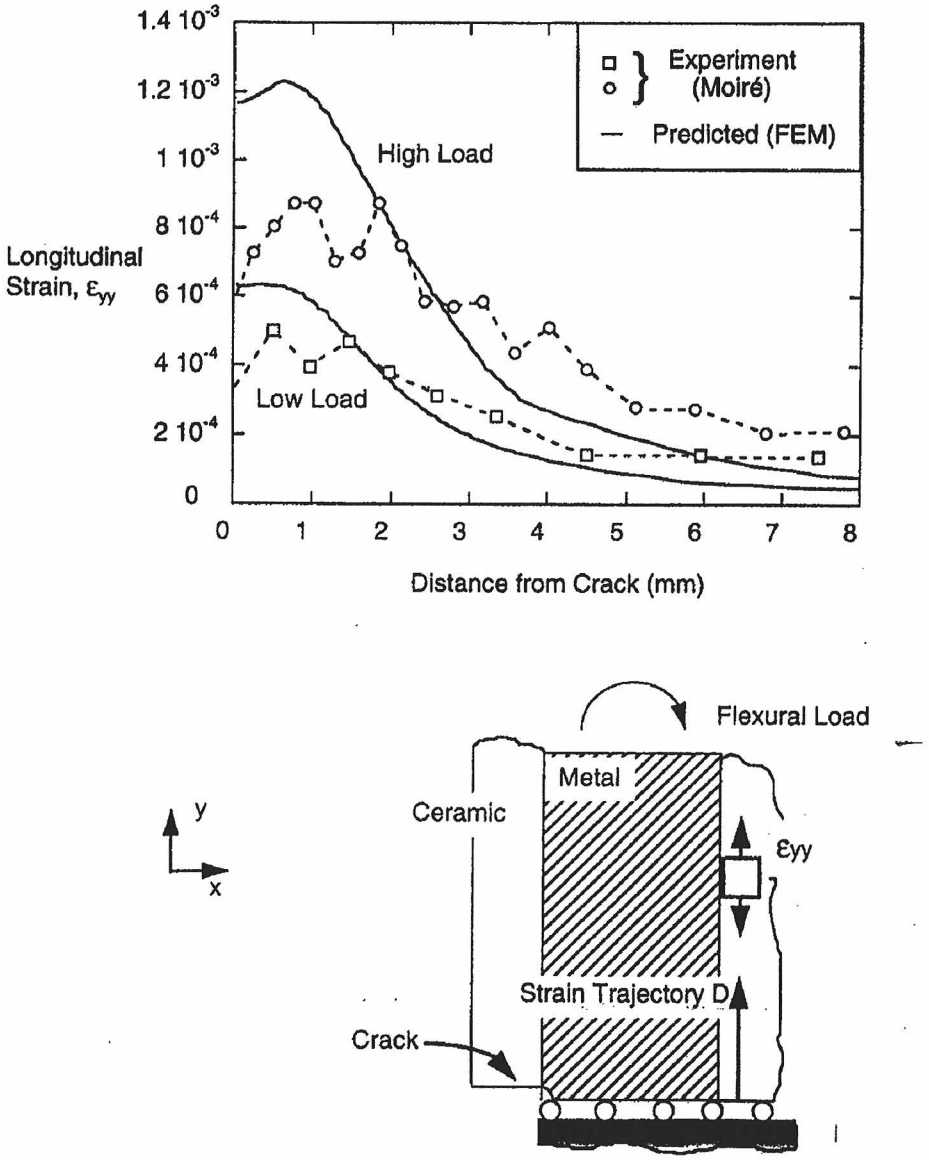

Fig. 6. Distributions of longitudinal strain, ε_{yy}, vs distance from the crack plane, y, within the intact ceramic layer ahead of the crack for applied bending moments of 1.5 and 2 Nm. Both experimental measurements and numerical predictions are shown.

3.1.2. *Flexural loading: finite element analysis.* The laminate specimen examined by moiré interferometry was modelled by finite element methods to allow direct comparison of the strain fields. The model geometry (dimensions and number of layers), material properties and boundary conditions were selected to agree with those of the specimens used for the moiré experiments described in Section 3.1.1. Specifically, the elastic moduli of the two materials were incorporated into the analyses (Table 2). An elastic–perfectly plastic constitutive law was ascribed to the metal layers in the model, with yield stress, σ_Y. In practice it is difficult to independently determine an appropriate value of σ_Y for the aluminium layers used in the experiments of Section 3.1.1. A value of σ_Y was therefore chosen to provide the best fit with experimentally determined strain fields. A single crack in the outermost ceramic layer directly opposite the middle roller was introduced. The crack tip was extended into the metal layer to a distance of 1/40 of the metal thickness, h_m, from the metal–ceramic interface with a finite crack tip radius of 1/40 h_m [Fig.7(a)]. This choice of crack tip geometry was based on experimental observations of crack tip profiles [Fig. 7(b)].

Flexural loading was applied to the finite element model by imposing a point load at the position of the upper load point in a horizontal direction. The magnitudes of the loads were chosen to coincide with those used during the moiré interferometry experiments. For each load level contour maps of the axial strain fields around the crack tip were determined. A typical contour map of the predicted axial strain is shown in Fig. 8 for an applied bending moment of 1.5 Nm and a metal yield strength of 50 MPa, which is typical of that for pure aluminium in the fully annealed condition as used experimentally (Appendix). The results indicate a localisation of axial strain near the tip of the precrack, with significant strain concentration extending in a direction perpendicular to the crack plane to a distance of several times the ceramic layer thickness. The strain distributions were determined along several different trajectories within this contour map. The results are compared with experimental distributions of strain obtained by moiré interferometry in Figs 4–7. Clearly, there is excellent agreement between the predicted and measured axial strain distributions. The agreement includes both the magnitudes of the strains and the distribution of strain around the crack tip at different loads.

The good agreement between the experimental and predicted ε_{yy} strain distributions in the layers near the tip of the crack (Figs 4–7) has several important implications. First, the assumption of a perfectly bonded interface must be valid. Second, plane strain conditions must be applicable. Third, the constitutive relationships of the materials, including an elastic–perfectly plastic response of the metal with a yield strength of 50 MPa appear to be well-represented. Finally, the crack tip geometrical

Table 2. *Properties of materials*

Material	Young's modulus, E (GPa)	Yield stress, σ_Y (MPa)	Poisson's ratio, ν
Alumina	380	—	0.2
Aluminium	70	50	0.3

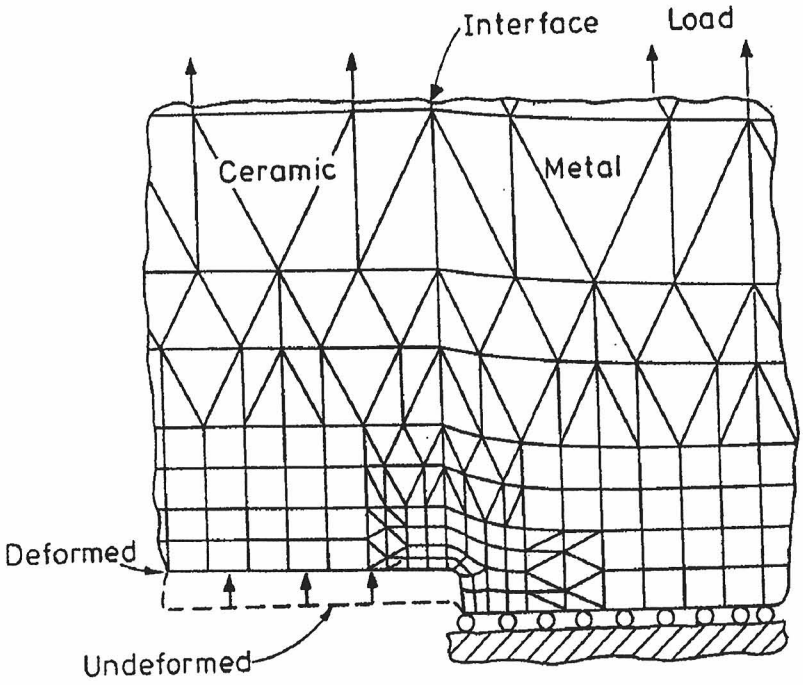

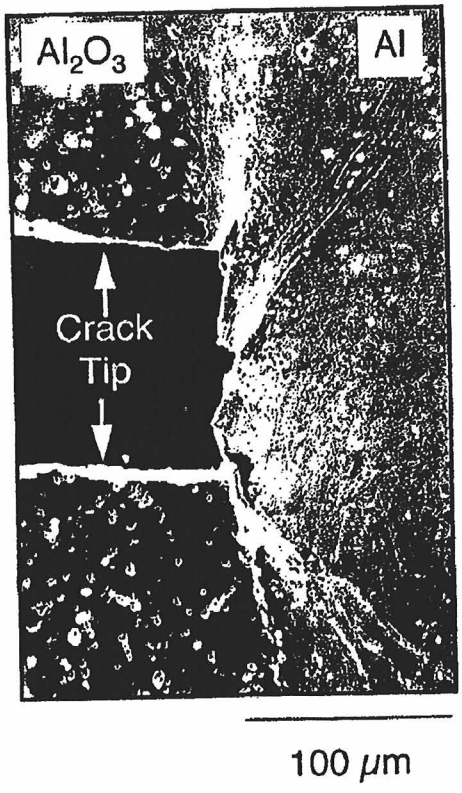

Fig. 7. An example of the crack tip mesh used in the finite element analyses. A high magnification scanning electron micrograph of a crack tip in an Al/Al_2O_3 laminate after a single load–unload cycle is shown for comparison.

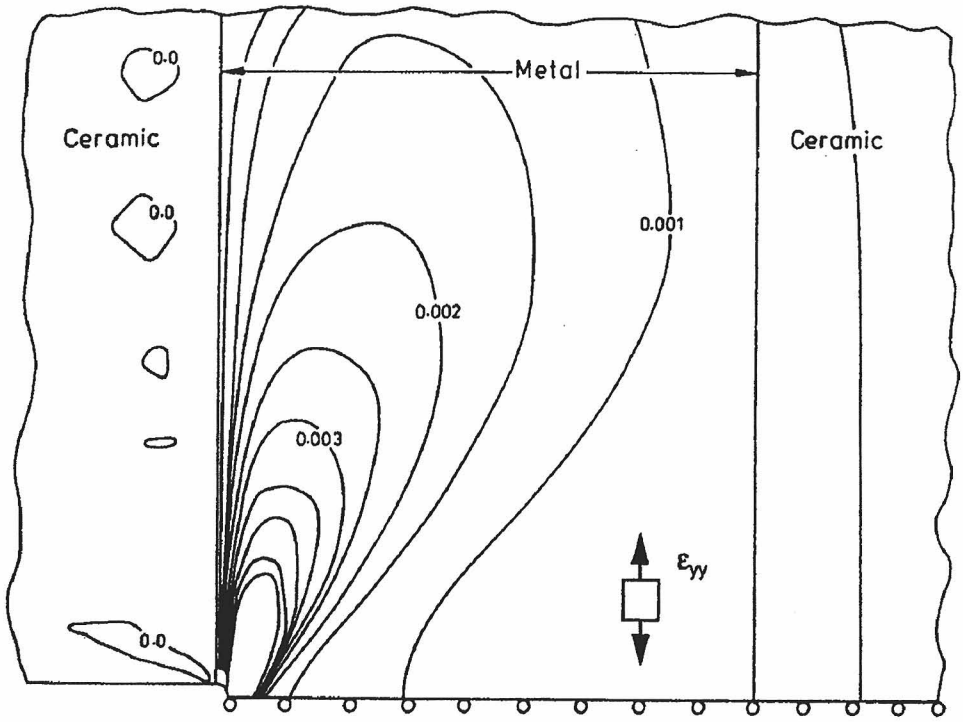

Fig. 8. A contour map of the predicted distribution of strain, ε_{yy}, in the vicinity of the crack tip showing a localisation of strain.

boundary conditions imposed appear to constitute a good approximation in this case. These conclusions then enabled the application of this modelling approach to the analysis of the precracked laminate geometry.

3.2. *Multiple crack geometry-remote tensile loading*

The distributions of stress near the cracks in the precracked geometry shown in Fig. 2(a) were investigated by finite element analysis using the unconstrained crack tip mesh geometry shown in Fig. 7(a). Tensile loads were applied by imposing a vertical displacement to the upper boundary of the model, which was constrained to remain straight. In other cases, the elastic crack tip displacement field was applied as a loading parameter by imposing the appropriate displacement boundary conditions to the perimeter of the precracked geometry. Stress components that were investigated included both the opening stress component, σ_{yy}, and the maximum principal stress, σ_1. The range of metal–ceramic layer thickness and precrack lengths used during the analyses are summarised in Table 3, whereas the material properties investigated were

Table 3. *Geometries of laminate microstructures analysed for fracture map*

Precrack length, a_0/h_c	1, 2, 5, 20, ∞
Metal–ceramic layer thickness ratio, h_m/h_c	1, 2, 4

the same as those for the flexural beam, except that now Young's modulus of both the ceramic and metal layers were assumed to be the same. For the analyses involving tensile loading, a range of remote tensile load, σ_∞, was applied, typically from $0 < \sigma_\infty < 2\sigma_Y$. Nodal displacements, strains and stresses were recorded at increments of $0.2\,\sigma_Y$.

In all cases, at low remote loads (e.g. $\sigma_\infty \sim 0.2\sigma_Y$), the entire system remained elastic, with the exception of small regions of the metal located near the tips of the cracks that exhibited plastic yielding. However, as the level of remote load was raised, plastic yielding of layers M1 and M2 resulted in a change in the distribution of axial stress, σ_{yy}, around the cracks. In some cases, this resulted in the location of peak axial stress moving from layer C1 to layer C2. This effect has strong implications for the predicted fracture response of these materials, as elaborated below.

An example of such a transition is shown in Fig. 9(a) and (b), where contour maps of the axial component of stress, σ_{yy}, obtained at two different loads ($\sigma_\infty/\sigma_Y = 0.2$ and 1, respectively), are presented from a laminate with equal thickness metal and ceramic layers and a precrack length of five ceramic and four metal layer thicknesses. In Fig. 9(a), the maximum axial stress in layer C2 is only of the order of $\sigma/\sigma_\infty \sim 1.2$, whereas for layer C1 the maximum axial stress reaches at least $\sigma/\sigma_\infty \sim 1.3$. Therefore, provided the ceramic layers exhibit a deterministic strength and provided the next crack will form at this level of remote load ($\sigma_\infty/\sigma_Y = 0.2$), a multiple cracking response is predicted since the location of the maximum stress occurs in layer C1. This might be expected to apply when the ratio of ceramic strength to metal flow stress is low (~ 1), for this layer thickness ratio and precrack length.

However, raising the magnitude of the remote load, such that significant plastic deformation of the metal layers occurred, led to a major redistribution of axial stress around the crack tip. This may be seen in Fig. 9(b), where a contour map of the same region shown in Fig 9(a) is illustrated, but for a remote load $\sigma_\infty/\sigma_Y \sim 1$. In Fig. 9(b), the location of peak axial stress now occurs in layer C2, which experiences a peak axial stress in excess of $\sigma_{yy}/\sigma_\infty = 2$. In contrast, the maximum axial stress in layer C1 is only of the order of $\sigma_{yy}/\sigma_\infty \sim 1.3$. The fact that the peak stress now occurs in layer C2 implies that fracture at this level of remote load ($\sigma_\infty/\sigma_Y \sim 1$) would proceed by dominant, single cracking, rather than the multiple cracking response predicted for the same geometry but at the lower load ($\sigma_\infty/\sigma_Y = 0.2$).

3.2.1. *Yielding of the bridging metal layer.* The observation that the location of peak axial stress depends on the ratio of the remote load to the yield stress of the metal is a direct result of plastic yielding of the bridging metal layer. Such yielding with increasing crack opening is well documented for constrained metal layers (Bannister and Ashby, 1991). Evidence of this phenomenon is shown in Fig. 10, which shows a plot of the average traction stress, $\bar{T}$, at the crack plane, in layer M1, against the average crack opening displacement, $\bar{u}$. The value of $\bar{T}$ is defined by

$$\bar{T} = \frac{1}{h_m}\int_0^{h_m} \sigma_{yy}(x, 0)\mathrm{d}x. \qquad (1)$$

Two broad regimes of the stress–displacement response of the metal layer may be distinguished. In the first stage, the metal layer acts essentially as a linear spring, such

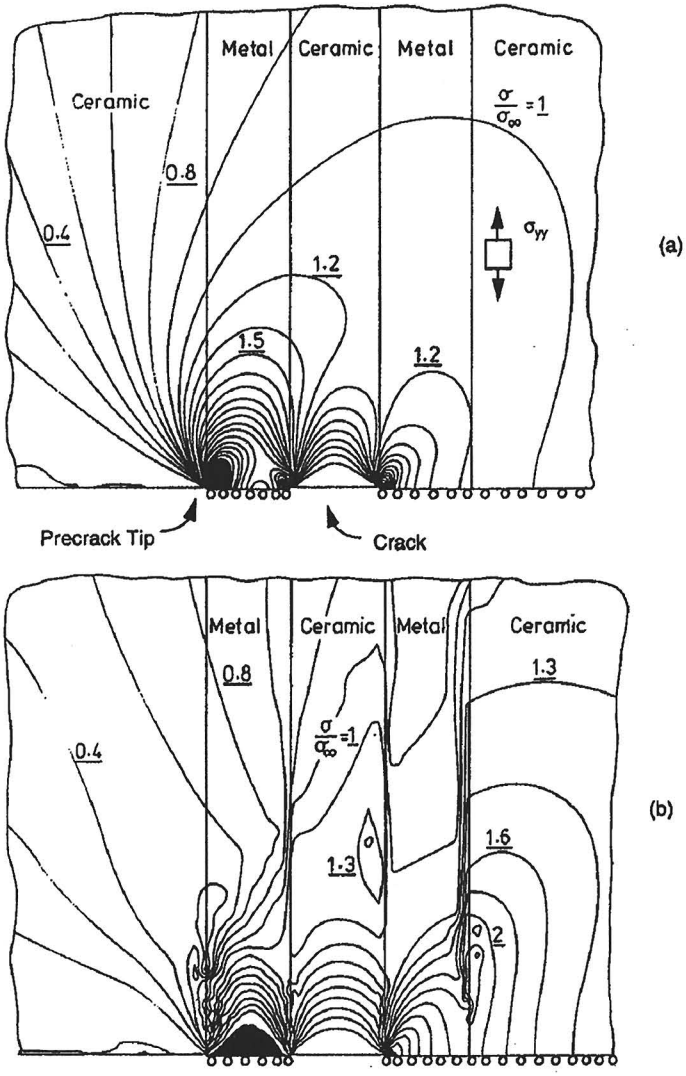

Fig. 9. Contour maps of the distributions of strain for a laminate containing equal thickness metal and ceramic layers and a normalised precrack of length of five. In (a), negligible plastic yielding has occurred, resulting in a maximum axial stress, σ_{yy}, occurring in layer C1. In (b), extensive plastic yielding has resulted in a shift in location of peak axial stress to layer C2.

that the increase in bridging traction is linear with average crack opening. In the second regime, however, significant plastic flow of the metal layer occurs and results in a sharp decrease in the rate of increase in bridging stress with crack opening. Furthermore, the magnitude of the normalised average crack opening displacement at which this transition occurs is dependent on the length of the precrack, a_0: longer precracks tend to result in higher stresses within the metal layer.

This effect, as well as the general observation of the bridging stress rising above the uniaxial yield stress, σ_Y, results from the high degree of plastic constraint imposed on the metal layers near the crack tip. This effect, in turn, is well known, and results from the presence of the stiff ceramic that is well bonded to either side of the metal layer

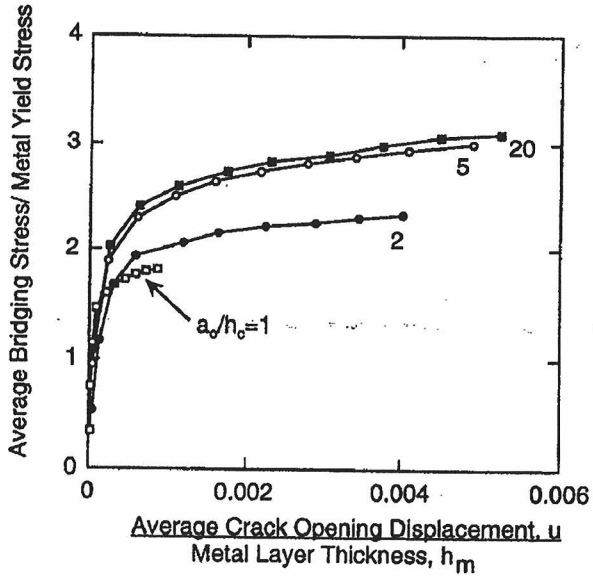

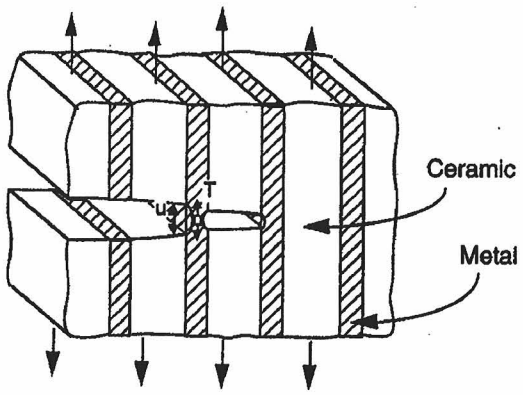

Fig. 10. Plot of the normalised average bridging stress, $\bar{T}/\sigma_Y$, vs average crack opening, $\bar{u}/h_m$ for several different precrack lengths.

(Hill, 1950). As a result, the magnitude of the applied stress required to bring the metal layer to the point of plastic yielding is raised, relative to the case with no constraint. The observation that the bridging stress is lower for shorter precracks now can be explained.

The high triaxiality near the crack tip results from transverse tensile stresses acting on the metal layer in directions parallel to the crack plane. These stresses originate (a) from the inability of the ceramic material on either side of the deforming metal layer near the crack tip to strain sufficiently in the x direction and (b) from the through thickness stresses generated by the plane strain condition. For materials with relatively short precracks, however, the magnitudes of the transverse, σ_{xx}, stresses that can build up within the cracked ceramic material are limited by the proximity of the free surface, as compared to the case of longer precracks. This effect then leads to

a decrease in the magnitude of the crack tip hydrostatic stress and consequent attainment of yield within the metal layer at lower applied stress, i.e. smaller crack openings. Thus, the maximum axial stress that can be carried by bridging metal layers is lower in systems with short precracks.

Yielding within layer M1 decreases the ratio of maximum wake stress to tip stress in two ways. First, the elastic contribution to the wake stress that arises from the surface tractions, $\bar{T}$, is linearly related to the magnitude of the traction stress (Roark, 1954). Once $\bar{T}$ reaches a maximum, a limit is placed upon the contribution to the wake stress from the corresponding traction on the crack flanks. Secondly, the crack tip stress intensity factor, as modified by the presence of the bridging metal layer is (Marshall *et al.*, 1985)

$$K_{tip} = 2\sqrt{\frac{a}{\pi}} \int_0^1 \frac{\sigma_\infty - T(X)}{\sqrt{(1-X^2)}} dX, \tag{2}$$

where X is the relative position along the crack flanks, $X = x/a_0$. Therefore, if the magnitude of T decreases relative to σ_∞, the increase in crack tip stress intensity factor will lead to an increase in the stress layer C2. Although (2) applies to semi-infinite half-space geometries with infinite cracks, these general trends should apply to the present situation.

Yielding within layer M2 does not significantly reduce the stress layer in C2, consistent with the findings of earlier analyses (Chan *et al.*, 1993). This conclusion was confirmed by comparing the results of an analysis with an elastic layer M2 ($\sigma_Y = \infty$) and elastic–plastic M1, to those of a similar analysis with elastic–plastic layers M1 and M2. No significant change in the distribution of stress within layer C2 was observed accompanying yielding of layer M1, between the two cases. This result indicates that the transition in fracture behaviour results primarily from a plateau in crack wake stress due to yielding of metal layer M1, as described above.

4. FRACTURE MAP FORMULATION

The stress distributions obtained from the finite element analyses at different loads have been used to formulate a fracture map for the failure mode of the composites. The maximum stress in the wake (σ_B^*) and in front of the crack (σ_A^*) were determined first from the distributions of stress within the layers at different increments of remote load for each composite system. These maxima were then normalised by the yield stress of the metal, σ_Y, and plotted against the normalised applied load (e.g. Fig. 11). In those cases when increasing the remote load caused the peak stress to shift from the crack wake to the region in front of the crack, the magnitude of the quantities were noted at this point (e.g. $\sigma_A^*/\sigma_Y = \sigma_B^*/\sigma_Y \sim 1.3$ in Fig. 11). These values were then plotted as the ordinate of a fracture map, with the corresponding metal to ceramic layer thickness ratio as the abscissa (Fig. 12).

This has the following physical interpretation: *if* the ratio of the fracture stress of the ceramic, σ_C, to the yield stress of the metal is fairly low (e.g. $\sigma_C/\sigma_Y < 0.7$ in Fig. 11), then the next crack that will form will do so when the level of the remote load is

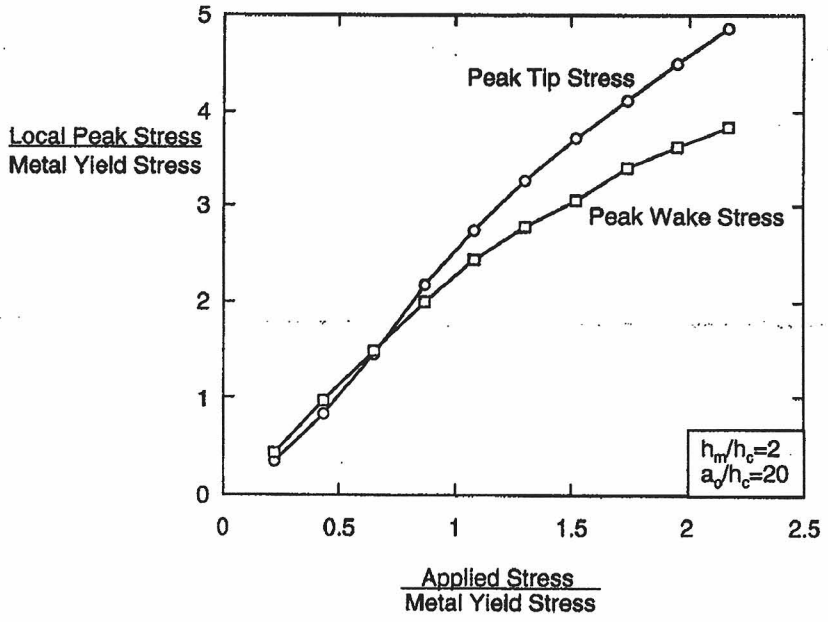

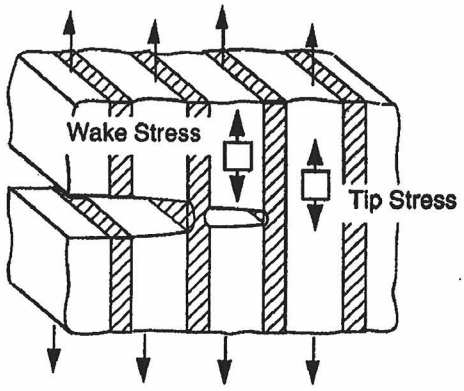

Fig. 11. Plot of the normalised peak axial stress in layers C1 (crack wake) and C2 (crack tip) vs the normalised applied stress.

such that insignificant yielding of the metal layer has occurred. Therefore, the appropriate stress distribution to be analysed is that corresponding to a nearly elastic system [Fig. 9(a)]. However, if the cracking stress to metal yield stress ratio is higher (e.g. $\sigma_C/\sigma_Y > 0.7$ in Fig. 11), then the remote load needed for further cracking is also higher, for given σ_Y, leading to a change from wake to frontal cracking in some cases [Fig. 9(b)]. These results are summarised in Fig. 12, which shows the results obtained from several different cases with different metal layer thickness and precrack lengths. Furthermore, this conclusion was valid if either the σ_1 or σ_{yy} component of stress was considered; there was less than 5% difference in the critical ratio of σ_C/σ_Y for either stress component.

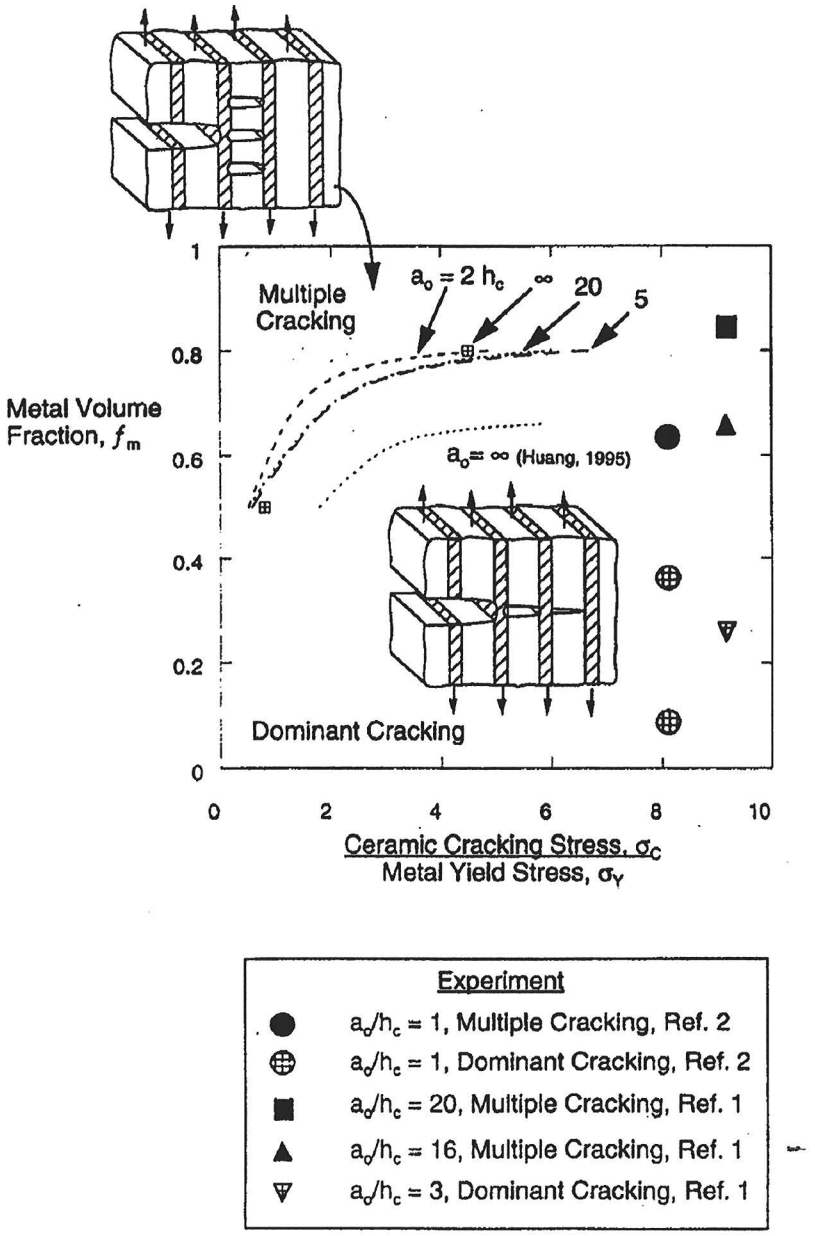

Fig. 12. Map of the predicted fracture mode for multilayers with different ratios of layer thickness and ceramic cracking stress to metal yield stress. σ_C/σ_Y.

It should be noted, however, that for laminates containing a precrack of length equal to one ceramic layer thickness, the location of maximum stress always occurred in the intact ceramic layer ahead of the crack tip, regardless of the level of remote load. In no instance was the maximum stress found to occur in the ceramic layer that already contained the crack. Therefore, in systems that do not contain a precrack of significant length, i.e. one that spans several layers, dominant cracking is the predicted failure mechanism. This prediction was found to apply to systems with the three layer thickness ratios that were investigated ($1 < h_m/h_c < 4$).

Comparison of the predicted fracture mode with experiment indicated good agreement for systems with long precracks and low and high metal volume fractions, and for systems with short precracks and low metal volume fractions but the prediction of an incorrect failure mode for systems with short precracks and high metal volume fractions. This can be seen in Fig. 12 where experimentally observed fracture modes (Shaw *et al.*, 1993; Pateras *et al.*, 1995) are included on the fracture diagram. Although the reasons for this discrepancy are not yet clear, it may be a consequence of the stochastic nature of brittle fracture. Further work to clarify this point is in progress (Shaw, 1995). Furthermore, these predictions for the mechanism boundary obtained by the finite element method differ from that identified by an elastic–plastic shear lag approach (Fig. 12) (Huang and Zhang 1995). The present analysis indicated that multiple cracking in systems with precracks of finite length will occur over a smaller range of layer thickness ratios. The cause of this discrepancy is not clear, although most likely arises in the different approaches used to conduct the analyses. This trend, however, is consistent with the general conclusion of the present investigation that wake stresses are decreased as a result of finite crack lengths, leading to a propensity towards dominant cracking.

5. CONCLUSIONS

A finite element model has been developed for investigating the fracture of ceramic–metal laminates. Moiré interferometry was used to investigate experimentally the distribution of strain surrounding cracks in aluminium/alumina laminates. Good agreement has been observed between the predicted and experimentally observed crack-tip strain fields. The finite element calculations were used to predict the fracture sequence of laminate specimens with precracks of varying lengths. These results have been used to develop a fracture map for prediction of the cracking patterns as a function of layer thickness, initial crack length and the ratio of ceramic strength to metal yield stress, σ_C/σ_Y. We find that fracture will tend to occur by dominant cracking for materials with relatively high ratios of σ_C/σ_Y. Experimental observations of crack patterns are in partial agreement with this prediction, although multiple cracking patterns have been observed at lower metal contents than predicted.

ACKNOWLEDGEMENTS

This work is part of a project supported by the EPSRC. The authors acknowledge many useful discussions with M. F. Ashby, W. J. Clegg and H. R. Shercliff.

REFERENCES

Bannister, M. and Ashby, M. F. (1991) The deformation and fracture of constrained metal sheets. *Acta Metall. Mater* 39, 2575–2582.

Chan, K. S., He, M. Y. and Hutchinson, J. W. (1993) Cracking and stress redistribution in ceramic/metal layered composites. *Mater. Sci. Engng* **A167**, 57–64

Hill, R. (1950) *The Mathematical Theory of Plasticity*. Oxford University Press, London.
Huang, Y., Zhang, H. W. (1995) The role of metal plasticity and interfacial strength in the cracking of metal/ceramic laminates. *Acta Metall. Mater.* **43**, 1523–1530.
Huang, Y., Zhang, H. W. and Wu, F. (1994). *Int. J. Solids Struct.* **31**, 2753.
Marshall, D. B., Cox, B. N. and Evans, A. G. (1985), The mechanics of matrix cracking in a brittle-matrix fiber composite. *Acta Metall. Mater.* **33**, 2013–2021.
Pateras, S. K., Shaw, M. C. *et al.* (1995) The effect of metal layer thickness on the fracture energy of metal/ceramic multilayers. *ICCM Conference Proceedings*, submitted.
Post, D. (1987) *Handbook on Experimental Mechanics*, pp. 314–387. Prentice-Hall.
Rasband, W. (1995) NIH Image, Anonymous FTP.
Shaw, M. C. (1995) The effects of strength probalistics on the fracture of metal/ceramic multilayers. *Acta Metall. Mater.*, submitted.
Shaw, M. C., Marshall, D. B., Dadkhah, M. S. *et al.* (1993) Cracking and damage mechanisms in ceramic/metal multilayers. *Acta Metall. Mater* **41**, 3311–3320
Roark, T. J. (1954) *Formulas for Stress and Strain*. McGraw-Hill, New York.

APPENDIX: MOIRÉ INTERFEROMETRY EXPERIMENTAL PROCEDURE

Bulk specimens were prepared by vacuum diffusion bonding stacks of commercially available alumina† and aluminium‡ sheets. The sheets were cleaned with acetone prior to bonding. Diffusion bonding was conducted in a vacuum of $\sim 10^{-5}$ Torr using an applied pressure of ~ 5 MPa at a temperature of 610°C for a time of 4 h. Beam specimens for the moiré interferometry experiments were cut from the diffusion bonded specimens using a water-cooled diamond abrasive cut-off saw. The dimensions of the beam were $\sim 5 \times h \times 100$ mm, where h depended on the metal layer thickness (Table 1). One side of the beams was polished using diamond metallographic compounds and a linear diffraction grating with 1200 lines/mm was reproduced on this side surface using epoxy resin. Three-point flexural testing of the laminate beams was conducted in displacement control. Loads were measured using an Entran 1 kN load cell with a load resolution of 1.8 N.

The surface strain states of the laminates were monitored during the experiment using moiré interferometry (Post, 1987). Two-beam interferometry was used with a 632 nm wavelength HeNe laser and an output power of 30 mW. This arrangement yielded moiré interferographs with a displacement sensitivity of 0.42 μm/fringe, with a possible strain resolution of $\sim 10^{-5}$. A typical experiment involved incrementally increasing the displacement of the loading points, followed by a pause during which the load was recorded and the interferographs were exposed and developed. The interferographs were digitised and the longitudinal fringe spacing, $L_0(y)$, were determined from the digitised images along longitudinal trajectories of interest using the public domain NIH Image program (Rasband, 1995). These fringe spacing were then used to calculate the longitudinal strains (ε_{yy}) (Post, 1987)

$$\varepsilon_{yy}(y) = \frac{}{2\nu L_0}, \tag{A.1}$$

where $\nu =$ the number of lines/mm in the diffraction grating.

† Hoescht alumina.
‡ Johnson-Matthey 99.999% aluminium.